Calce et malleo
Mésszel és kalapáccsal

12. KŐZETTANI ÉS GEOKÉMIAI
VÁNDORGYŰLÉS

Calce et malleo – Mésszel és kalapáccsal

12. KŐZETTANI ÉS GEOKÉMIAI
VÁNDORGYŰLÉS

A kötetben közölt cikkek tartalmáért a szerzők vállalják a szakmai felelősséget.

Szerkesztette:
Fehér Béla, Molnár Kata, Lukács Réka, Czuppon György és Kereskényi Erika

Lektorok:
Molnár Kata, Lukács Réka, Czuppon György és Kereskényi Erika

Kiadja a Csillagászati és Földtudományi Kutatóközpont, Földtani és Geokémiai Intézet

Felelős kiadó:
Kiss László
főigazgató

ISBN 978-963-7331-00-8

Címlapkép:
Részlet a Rákóczi 1. sz. barlangból, Tornaszentandrás, Esztramos-hegy
Fotó: Czuppon György

Calce et malleo – Mésszel és kalapáccsal

12. Kőzettani és Geokémiai Vándorgyűlés
Miskolc, 2022. szeptember 22–24.

Szerkesztette:

Fehér Béla
Herman Ottó Múzeum, Ásványtár, Miskolc

Molnár Kata
Atommagkutató Intézet, Izotópklimatológiai és Környezetkutató Központ, Debrecen

Lukács Réka
ELKH, Csillagászati és Földtudományi Kutatóközpont, Földtani és Geokémiai Intézet, Budapest
CSFK, MTA Kiváló Kutatóhely, Budapest
MTA-ELTE Vulkanológiai Kutatócsoport, Budapest

Czuppon György
ELKH, Csillagászati és Földtudományi Kutatóközpont, Földtani és Geokémiai Intézet, Budapest
CSFK, MTA Kiváló Kutatóhely, Budapest

Kereskényi Erika
Herman Ottó Múzeum, Ásványtár, Miskolc

Budapest, 2022

12. Kőzettani és Geokémiai Vándorgyűlés
Miskolc, 2022. szeptember 22–24.
Helyszín: MTA Miskolci Akadémiai Bizottság székháza
3530 Miskolc, Erzsébet tér 3.

Rendezők

Csillagászati és Földtudományi Kutatóközpont, Földtani és Geokémiai Intézet
Herman Ottó Múzeum, Ásványtár
Aggteleki Nemzeti Park Igazgatóság
Miskolci Egyetem, Ásványtani-Földtani Intézet
Magyarhoni Földtani Társulat
MTA Miskolci Akadémiai Bizottság

Szervezőbizottság

Czuppon György (főszervező, CSFK, FGI)
Kereskényi Erika (főszervező, HOM)
Lukács Réka (CSFK, FGI; MTA-ELTE VKCS)
Molnár Kata (ATOMKI)

Támogatóink

Laborexport Kft., Per-Form Hungaria Kft., Carl Zeiss Technika Kft., JEOL (Europe) SAS, Auro-Science Consulting Kft., Nanotest Hungary Kft., Unicam Magyarország Kft., Isotoptech Zrt. és Austro-Lab Kft.

TARTALOM

Fehér B., Molnár K., Lukács R., Czuppon Gy. & Kereskényi E. (szerk.) (2022): Calce et malleo – Mésszel és kalapáccsal. 12. Kőzettani és Geokémiai Vándorgyűlés. CSFK Földtani és Geokémiai Intézet, Budapest. ISBN 978-963-7331-00-8

TEMPERATURE-FLUID CHEMICAL CONDITIONS OF MASSIVE MONAZITE FORMATION OF REE-RICH VEINS IN JOLOTCA (ROMANIA)

Krisztián Fintor[1]*, Heléna Guba-Walter[1], Luca Kiri[1], Ferenc Kristály[2] & Elemér Pál-Molnár[1]
[1] Department of Mineralogy, Geochemistry and Petrology, University of Szeged, Szeged, Hungary
[2] Institute of Mineralogy and Geology, University of Miskolc, Miskolc, Hungary
* E-mail: fintor.krisztian@szte.hu

1 Introduction

The Ditrău Alkaline Massif (DAM) is located in the Eastern Carpathians (Romania) and has been identified as a potential rare earth element (REE) deposit in the European Rare Earth Potential Assessment Programme (Goodenough et al., 2016). The DAM is a petrographically and structurally diverse alkaline igneous complex that is intruded into metamorphic rocks of the Eastern Carpathians during the Middle–Late Triassic (Ladinian–Norian) (Pál-Molnár et al., 2021).

The northern area of the DAM is the most important for REE deposits, where a series of ultramafic and mafic rocks gradually shifts towards more felsic compositions from West to East. Rare-earth ores are present in the form of mineralised veins, the most significant of which are located at the Jolotca ore field, where E–W trending, north dipping veins vary between a few hundred meters to one kilometre, their width is 5–150 cm but occasionally it may reach up to 20 m (Jakab & Garbaşevschi, 1976). Mineralised veins of Jolotca intersect the ultramafic and mafic rocks and there is no genetic relationship between the host rocks and the veins.

The Jolotca ore field hosts minerals enriched in LREE where the typical REE-minerals are REE(Y)-phosphates; LREE(Y)-carbonates; Nb, Ta, REE(Y), Ti, Fe oxides; REE-(Y)-Th-Zr silicates among others (Hîrtopanu, 2018). Besides these, sulphide ores (e. g. pyrite, sphalerite, galena, molybdenite) are common, as well as carbonates (e. g. siderite, ferroan dolomite, ankerite, calcite) and occasionally quartz occur as barren minerals (Hîrtopanu, 2018).

In the ore veins of the Jolotca area, monazite-(Ce) is a dominant constituent REE mineral accompanied by apatite, allanite-(Ce) and bastnäsite-(Ce), while xenotime-(Y) is present only as an accessory phase.

In this work we try to clarify the position of monazite in the paragenetic sequence. Furthermore, by chemical analysis of monazite and xenotime and by examining the fluid inclusions trapped in the monazite, we try to reveal what temperature and fluid chemical conditions were characteristic during the formation of monazite.

2 Materials and methods

Samples were characterized at the University of Szeged, using an Olympus BX41 polarization microscope. Chatodoluminescence (CL) analyses were performed with a Reliotron cold cathode instrument. Conditions during CL imagery, were 7 kV beam voltage and 0.670 mA valve current. BSE images were taken by an AMRAY 1830 scanning electron microscope (acc. voltage: 20 kV, beam current: 10 μA) at the Eötvös Loránd University. EDS X-ray element maps were made at University of Miskolc by a JEOL JXA-8600 Superprobe (20 kV acceleration voltage, 20 nA probe current).

Mineral compositions were measured using a JEOL JXA 8200 Suberprobe at the Montanuniversität Leoben Austria. Measurement settings were 20 kV accelerating voltage and 10 nA beam current. Detection limit was < 0.01–0.03% in case of Al, Si, Ca, P, Zr, and 0.02–0.07% for REEs (HREE+LREE) while 0.01–0.07% for U, Th and Pb.

Raman spectroscopy was performed with a Thermo Scientific DXR confocal Raman microscope at the University of Szeged. Analyses were made by a diode pumped solid state (DPSS) frequency-doubled Nd-YAG laser with an excitation wavelength of $\lambda = 532.2$ nm.

Microthermometric measurements were carried out with a Linkam MDSG600 motorized heating-freezing stage operating over a temperature range from –190 to 600 °C. Calibration was done by using synthetic fluid inclusions with melting of CO_2 at –56.6 °C (triple point), melting of water at 0.0 °C (triple point) and the critical homogenization temperature of water at 374.0 °C. The accuracy of obtained data is approximately ±0.2 °C under freezing and ±0.5 °C under heating conditions.

Fluid compositions and molar volumes have been calculated with the computer program "AqSo2e" and "BULK" from software package "FLUIDS" and "ICE" from the software package "CLATHRATES" (Bakker, 1997), using the equation of state from Chueh & Prausnitz (1967).

3 Results

3.1 Petrography

The structure of mineralised veins is often chaotic, made up by anastomosing veins and vein swarms. Brecciated fragmented mineral assemblages occur frequently, especially in the sulphide dominant part of the veins. Samples with a banded appearance and definite shear marks are also observed.

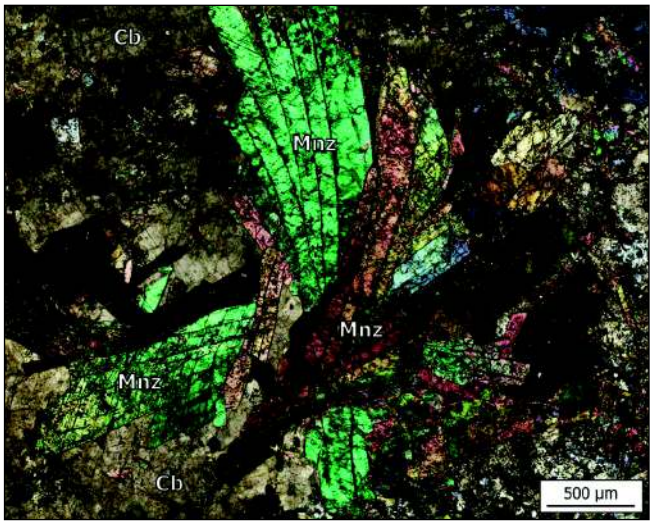

Fig. 1: *Fan-shaped monazite crystals (Mnz) in carbonate (Cb) matrix.*

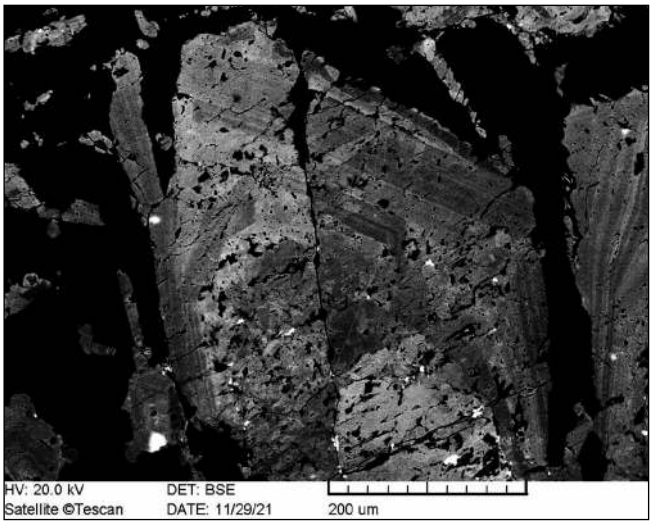

Fig. 2: *Complex internal zonation of a columnar crystal occurring in a well-developed fan-shaped monazite crystal aggregate.*

The most prominent mineral in the vein network is monazite (group), which appears in the form of veins from a few mm to dm in thickness. Aggregates of radially arranged long prismatic crystals (fan-shaped crystal aggregates) that can reach a cm in their largest dimension, is one of the most common forms of appearance of monazite (Fig. 1).

Monazite crystals have a complex internal texture. Oscillatory zoning, discontinuous rims or thin veinlets can be found as frequently as patchy- and convolute zonation (Fig. 2). Anhedral hematite together with minor thorite can be found frequently as solid inclusion clusters of distinct domains of the monazite grains.

Dissolution and alteration features mainly appear as pseudomorphic substitution of a monazite crystal by bright lemon-yellow CL coloured apatite. Other remarkable alteration product is a needle-like allanite crown on the surface of monazite grains with significant dissolution patterns of the original monazite.

Xenotime occurs as scattered clusters of tiny euhedral crystals arranged interstitially among monazite, or as bulk anhedral crystals with frequent contact with monazite grains. The contact between monazite and xenotime is always sharp without any dissolution features or reaction fronts. Concentric oscillatory zonation is observable in the tiny ones while irregular patchy zonation is characteristic in the bulky anhedral xenotime crystals.

The other phosphate phase present in large amounts is apatite, which consists of bulk aggregates of euhedral crystals and shows advanced signs of resorption. Internal texture of apatite aggregates is very turbid, irregularly shaped inclusion-free domains can be found only in the core of a few large crystals. CL imagery highlights the dual internal structure of apatite, by brownish CL colour of inclusion free cores and bright lemon yellow colour of the heavily turbid parts.

Allanite occurs in a variety of forms, often as radially oriented single crystal clusters, but also as flaky grains in carbonate and on the surface of columnar hydroxyl bastnäsite crystals and as a partial substitute of the mineral. It can also be observed in the intersecting veins of monazite, where it is associated with lemon yellow CL-coloured apatite and as a product of alteration on monazite, but only where the monazite is in contact with chlorite, serving as Si source.

The sulphides are predominantly pyrite, one type being massive and often fractured into brecciated-like fragments, the other type consists of clusters of hexahedral crystals and occurs in veins filled with chlorite and carbonate. Sphalerite is associated with breccia-like bulky pyrite and appears as an anhedral highly resorbed phase.

Chlorite can be observed as greenish coloured, vermicular nodules and is most commonly found in leaching cavities of carbonates, associated with quartz in thin veins, or in masses in shear zones.

Four carbonate generations have been distinguished, with siderite and Sr-ankerite being the most abundant. Siderite has a massive habit and in many places only occur as strongly resorbed relicts. Places among resorbed siderite are filled by bulk Sr-ankerite. In places the Sr-ankerite is replaced by dull red CL coloured Mn-calcite. In thin veins intersecting all other carbonates and, less frequently, in small pools between other carbonates, dark orange CL-coloured calcite is observed.

3.2 Chemical composition of monazite and xenotime

WDS element mapping of different type of monazite crystals showed that the distinctive zonation observed in BSE images are caused by differences in Th concentration. In Th-rich parts, there is a slight enrichment in concentration distribution of Ca, Si an Fe are also observable. The thorium content ranges from ~1–4 wt.% expressed as ThO_2, while the uranium content is mostly below the detection limit, where it is detectable the UO_2 content is < 0.1 wt.%. Microprobe point analyses revealed that every analysed monazite grain is Ce-dominant, and their chondrite-normalised REE distribution exhibit La > Ce > Eu > Nd > Pr > Sm relative trend without

negative Eu anomaly. Their Y_2O_3 content is very low and varies between 0.1 and 0.6 wt.%.

In xenotime grains, the zonation seen in BSE images are caused by differences in the distribution of HREE elements, especially Gd (0.05–0.1 *apfu*), Eu (0.00.2–0.01 *apfu*) and Yb (0.02–0.03 *apfu*).

3.3 Fluid inclusion study in monazite host

Basically two main fluid inclusion populations could be distinguished on the basis of their intra-crystal arrangement. Population 1 is represented by solitary inclusions with random distribution in the host crystal. Fluid inclusions of population 1 are supposed to be primary in origin based on their petrographic characteristics. Inclusions of the fluid inclusion population 2 form fluid inclusion trails that are arranged along healed micro cracks and are completely extended until the crystal boundaries. The petrographic features of fluid inclusion population 2 indicate their secondary origin.

The inclusions of the two populations show very similar characteristics, ranging in size from 2 to 10 µm, with the vast majority being irregularly shaped and two-phased (LV) with fluid dominancy (φ_{vap}: 0.1–0.3) at room temperature. There are three fluid types present both in the primary and secondary originated inclusions.

The majority of the inclusions contain aqueous carbonic fluid with gaseous CO_2 in the vapour phase and NaCl as major dissolved salt. The initial melting temperature (T_i: ~–23 °C) is indicative of a H_2O-NaCl-CO_2 type fluid. T_m (Ice) values are between –18.5 and –4.5 °C (Fig. 3) and T_m (Cla) values are between –5.5 and 6.5 °C, suggesting a fluid composition of 12–21 mass% $NaCl_{eq.}$ salinity and 2–4 mol% CO_2. All of the inclusions homogenize into the liquid phase (LV to L) without exception. Vast majority (> 90%) of Th values are in a 223 to 330 °C range with median value of 267 °C (Fig. 3).

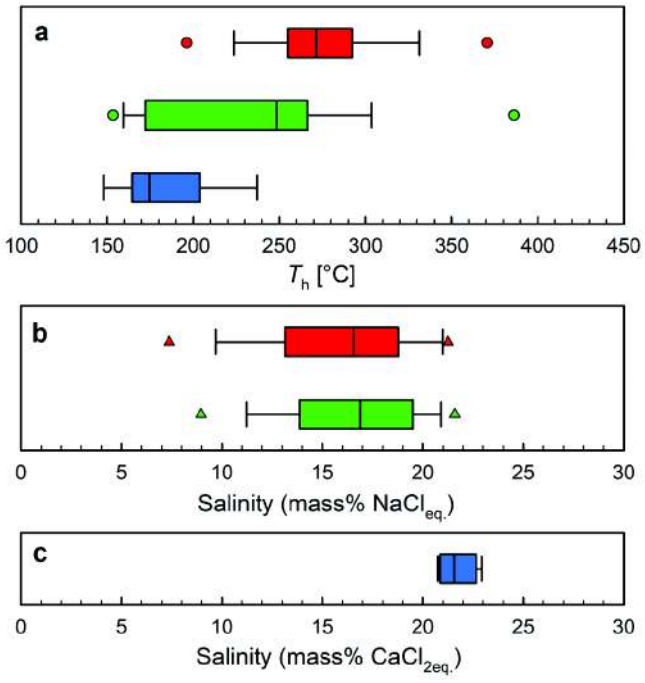

Fig. 3: *Microthermometry results of primary fluid inclusions. a) T_h data; b, c) Salinity data. Legends: red: H_2O-NaCl-CO_2 fluid; green: H_2O-NaCl fluid; blue: H_2O-NaCl-$CaCl_2$ fluid*

The second most common type of fluid is an aqueous electrolyte type fluid; which composition differs from the aqueous-carbonic one mainly in the absence of CO_2. This fluid type can be modelled in the H_2O-NaCl system (T_i: –23 to –21 °C) and exhibiting 7–22 mass% $NaCl_{eq.}$ salinity. The fluid also homogenizes into the liquid phase during heating, in a bit broader 160 to 304 °C range, with a median value of 251 °C (Fig. 3).

The third type of fluid represents the smallest proportion. It is also an aqueous electrolyte system, but in addition to NaCl it also contains $CaCl_2$, as indicated by the first melt phase already appearing below –40 °C.

T_m (Ice) values are in a –20.3 to –25.3 °C range (Fig. 3). The fluid can be described by the H_2O-NaCl-$CaCl_2$ model system, but in the absence of T_m (Hh) values, a composite salinity cannot be given, so its salinity ranges from 20.7–23 mass% $CaCl_{eq.}$ in the H_2O-$CaCl_2$ system. Homogenization of this fluid also occurred into the liquid phase in a 148 to 237 °C T_h range where the median value is 174 °C (Fig. 3).

4 Discussion and conclusions

For the purpose of determining the origin of monazite crystals, their mineral chemistry was used as a basis. A multivariate statistical classification algorithm, linear discriminant analysis was applied in order to separate monazites of different origin. The procedure used a large amount of monazite data from the literature with the most diverse genetics possible (Wu et al., 2019 and references therein). The best possible separation was achieved by using the La, Ce, Sm, Gd, Ca, Si, U and Th contents of the monazites as predictive variables, which gave a 98% probability that our analysed monazite is of hydrothermal origin.

The chemical composition of xenotim is also indicative of the conditions under which they were formed, their Gd_N (12–24 wt.%) and Eu_N (2–12 wt.%) values suggest that they crystallised from an aqueous fluid.

Since contact between monazite and xenotime phases is generally sharp, without any reaction fronts or dissolution features, indicate that the two minerals were in equilibrium during their formation. Y-content of monazite which is in equilibrium with xenotime is used to estimate the p-T parameters of monazite-xenotime mineral assemblages during their formation (Gratz & Heinrich, 1997). The solvi used to estimate the formation temperature range were calculated for two limiting pressures [0.1 MPa and 700 MPa (Pál-Molnár et al., 2015)] using the equations of Mogilevsky (2007). A range of 245 ± 14 to 396 ± 17 °C can be estimated for monazite crystallization temperature (Fig. 4).

Petrographic results show that the beginning of the hydrothermal stage of vein mineralization is represented by the formation of fan-shaped monazites. Following the monazite formation (partly overlapping it), small amounts of xenotime was generated, followed by massive apatite deposition. The precipitation of early sulphides (e.g. pyrite, sphalerite) was followed by phosphate mineralisation.

The developed mineral assemblage was affected by pervasive metasomatism. Signs of this effect can be seen beyond the dissolved surfaces of the monazite and xenotime crystals, in their patchy, sometimes chaotic internal zonation. But the most extensive alteration is seen in apatite, where relicts of the original apatite can still be seen as resorbed islands, but much of the mineral has been replaced by dissolution-reprecipitation by a new apatite phase.

The dissolution and reprecipitation is observed on monazite also, which is a well-documented process common in low-temperature (< 400 °C) metamorphic or hydrothermal conditions (Townsend et al., 2000; Rasmussen & Muhling, 2007). Th-rich monazites tend to dissolve at low temperatures, resulting in the formation of new monazite rich in thorite and hematite inclusions (Rasmussen & Muhling, 2007), similar to our observations.

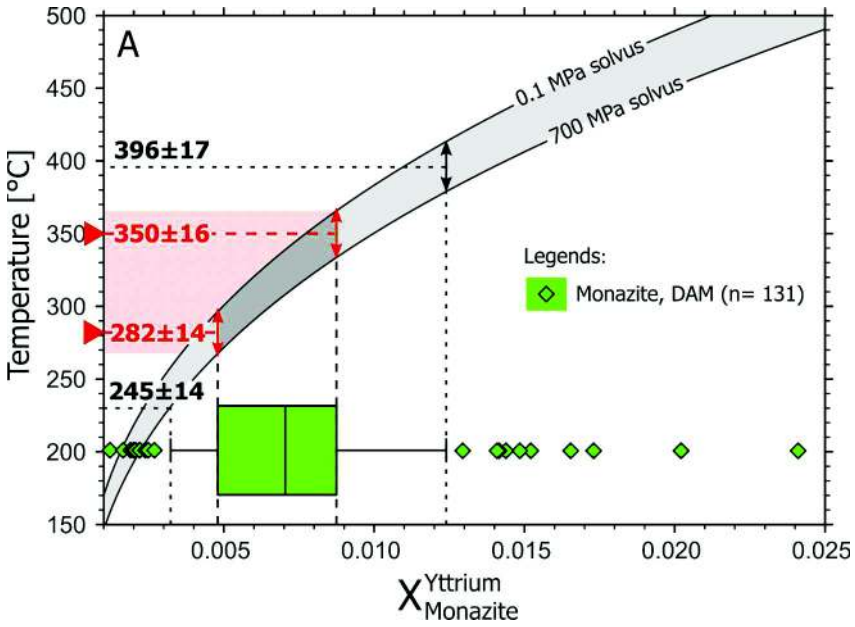

Fig. 4: *Temperatures estimated by Y in monazite thermometry.*

The broad salinity ranges (7–22 mass% $NaCl_{eq.}$, Fig. 3/b) in H_2O-NaCl-CO_2 and H_2O-NaCl fluids could be a result of mixing of fluids with different salinity (Dubessy et al., 2003). The main difference between composition of these two types of fluids is the CO_2 content, however lack of volatile content can be explained by effervescence following a sudden pressure drop. Pressure fluctuations associated with fracture opening and sealing are very common phenomena in active hydrothermal systems. Traces of displacement-related crack opening and re-cementation are abundant in the vein system, supported by the presence of many brecciated vein texture and markers of shearing processes.

The appearance of $CaCl_2$ in the fluid indicates a change in the Ca/Na balance of the fluid system. The increasing Ca ratio favours allanite formation, especially in progressive processes (e.g., metasomatism), where it often appears together with apatite at the expense of monazite (Janots et al., 2008). This type of allanitization is observed in our case and can be brought into line with the changes in fluid chemistry.

Further studies are needed to decide to what extent estimated temperatures represent the original formation conditions or a metasomatic overprinting.

Acknowledgement

This research was supported by the National Research Development and Innovation Office – NKFIH, 135089.

References

Bakker, R. J. (1997): Computers & Geosciences, 23, 1–18.

Chueh, P. L. & Prausnitz, J. M. (1967): Industrial & Engineering Chemistry Fundamentals, 6, 492–498.

Dubessy, J., Derome, D. & Sausse, J. (2003): Chemical Geology, 194, 25–39.

Goodenough, K. M., Schilling, J., Jonsson, E., Kalvig, P., Charles, N., Tuduri, J. Deady, E. A., Sadeghi, M., Schiellerup, H., Müller, A., Bertrand, G., Arvanitidis, N., Eliopoulos, D. G., Shaw, R. A., Thrane, K. & Keulen, N. (2016): Ore Geology Reviews, 72/1, 838–856.

Gratz, R. & Heinrich, W. (1997): American Mineralogist, 82, 772–780.

Hîrtopanu, P. (2018): In: Hîrtopanu, P. (Ed.): New minerals and mineral varieties for Romania. Vergiliu, pp. 97–150.

Jakab, Gy. & Garbaşevschi, N. (1976): Dări de seamă ale şedinţelor, 63/2, 13–25.

Janots, E., Engi, M., Berger, A., Allaz, J., Schwarz, J.-O. & Spandler, C. (2008): Journal of Metamorphic Geology, 26, 509–526.

Mogilevsky, P. (2007): Physics and Chemistry of Minerals, 34, 201–214.

Pál-Molnár, E., Batki, A., Almási, E., Kiss, B., Upton, B. G. J., Markl, G., Odling, N. & Harangi, Sz. (2015): Lithos, 239, 1–18.

Pál-Molnár, E., Kiri, L., Lukács, R., Dunkl, I., Batki, A., Szemerédi, M., Almási, E. E., Sogrik, E. & Harangi, Sz. (2021): Central European Geology, 64, 18–37.

Rasmussen, B. & Muhling, J. R. (2007): Contributions to Mineralogy and Petrology, 154, 675–689.

Townsend, K. J., Miller, C. F., D'Andrea, J. L., Ayers, J. C., Harrison, T. M. & Coath, C. D. (2000): Chemical Geology, 172, 95–112.

Wu, L.-G., Li, X.-H., Ling, X.-X., Yang, Y.-H., Li, C.-F., Li, Y.-L., Mao, Q., Li, Q.-L. & Putlitz, B. (2019): Minerals, 9, 583.